Reduction of recombination rates due to volume increasing, annealing, and tetraethoxysilicate treatment in hematite thin films

S. Congolo[1,*], M.J. Madito[2,*], A.T. Paradzah[1], A.J. Harrison[1], H.M.A.M. Elnour[1], T.P.J. Krüger[1], M. Diale[1]

[1] Department of Physics, University of Pretoria, Pretoria, 0002, South Africa

[2] iThemba LABS, National Research Foundation, Somerset West, PO Box 722, Cape Town, 7129, South Africa

*Correspondence to S. Congolo (sipho.congolo@gmail.com) or M. J. Madito (mmadito@tlabs.ac.za).

Abstract

We report on the properties of hematite thin films prepared by spray pyrolysis on fluorine-doped tin oxide (FTO)-coated glass substrates and investigated the effect of the spray volume, tetraethoxysilicate treatment of the hematite, and post-annealing at 500 °C for 2 h with 10 °C/min ramping. Raman spectroscopy confirmed the characteristic Raman spectrum of all the films, while high-resolution confocal Raman microscopy showed a uniform intensity, suggesting a homogeneous coating of the hematite films on the FTO substrates. Ultrafast transient absorption spectroscopy indicates that all three experimental parameters—a larger spray volume, tetraethoxysilicate treatment, and annealing—slowed down electron–hole recombination. Global analysis of the difference absorption data resolved the spectra and associated decay lifetimes of three distinct processes, operating on the ultrafast, tens of picoseconds, and hundreds of picoseconds timescales.

Keywords: Hematite; FTO; Raman depth profiles; Absorption analysis; Spray pyrolysis

Introduction

The need for more energy has inevitably led to environmental issues such as global warming due to the increased burning of fossil fuels which release greenhouse gases. The total global power demand is currently ~17.4 TW (Seger and General 2016). The world energy consumption will undoubtedly increase every year, and that is why, we need renewable and sustainable energy. Solar radiation is the most abundant, clean, and renewable source of energy on Earth. A total of ~ 104 TW of solar irradiation reach the Earth's surface, which greatly surpasses our demand for energy (Cho 2010). Scientists have focused much of their efforts on investigating nanostructured semiconductor materials as photoanodes for photoelectrochemical water splitting to produce hydrogen and oxygen as biofuels. Nanostructured iron oxides have attracted much attention as a low-cost environmentally friendly material for multiple applications in different technological areas, such as microwave absorption, catalysis, gas sensors, magnetic storage, clinical diagnosis and treatment, etc. (Tadic et al. 2019). Generally, nanostructures have been used to fabricate high-performance nanotwinned surfaces for the mechanical industry (Zhang et al. 2017a), and nanoparticles have been applied to develop novel environment-friendly slurries for high-performance devices used in aerospace, energy, semiconductor, and power industries contributing to the

conventional manufacturing technologies (Zhang et al. 2019, 2018, 2017b, 2012; Wang et al. 2018).

Hematite (α-Fe_2O_3) has over the years received much publicity as a potential applicant as a semiconductor material for photoelectrochemical cells (PEC) in solar water splitting, with a high theoretical maximum efficiency of 12.9% (Kumari et al. 2010). This electrochemically stable compound is attractive due to its relative abundance, narrow band gap (1.9–2.3 eV) which allows for absorption of ~ 40% in the visible region of the solar spectrum, low production cost, and non-toxicity (Kumari et al. 2010; Huang et al. 2012). These properties put α-Fe_2O_3 ahead of the other photoactive material that have been investigated as potential photoanodes in PEC such as bismuth vanadate ($BiVO_4$), anatase (TiO_2), tungsten trioxide (WO_3), and zinc oxide (ZnO) (Huang et al. 2012; Iandolo et al. 2015; Cho et al. 2015; Dare-Edwards et al. 1983). However, hematite has a few drawbacks: its low conductivity and exceptional short hole diffusion length of 2–4 nm impede charge transport and, as a result, lead to a high recombination rate of photo-generated carriers (Iandolo et al. 2015; Cho et al. 2015). To overcome these shortcomings, some research has focused on surface treatment of hematite to improve the material's properties. Methods such as synthesis of nanostructured hematite including nanowires and nanorods (Satsangi et al. 2008; Beermann et al. 2000), incorporation of host–guest heterostructures (Wang et al. 2014; Shinde et al. 2016), elemental doping, and heat treatment (Kim et al. 2013; Shen et al. 2013; Wang et al. 2015; Hahn and Mullins 2010) have been employed. The use of synthesised hematite nanostructures allows for efficient transport and collection of photoexcited electrons through a given path. Furthermore, such structures offer enhanced photoresponse for application in solar water splitting. Host (or underlayer material) has also shown to significantly improve the efficiency of hematite in water oxidation (Paradzah et al. 2017; Miyake and Kozuka 2005; Hisatomi et al. 2012; Kang and Kang 2015). The host material increases the photocurrent density through diffusion doping and reduces the recombination of electrons at the fluorine-doped tin oxide (FTO)/hematite interface. This, in turn, increases the hole lifetimes. In photoelectrochemical water splitting, the holes are then involved in the oxidation of water to produce O_2 molecules and H^+ ions. The electrons are transported to the counter electrode where they are involved in the reduction of the H^+ ions to produce the hydrogen gas that is used as a fuel. It is, therefore, imperative that increased electron–hole recombination rates greatly deplete the concentration of electrons and holes leading to minimal redox processes.

Elemental doping is another promising method that has been used to enhance the chemical and optical properties of α-Fe_2O_3. Hematite doped with elements such as titanium, tin, and silicon has shown to have an increased photocurrent density and reduced electron–hole recombination due to an increase in donor density (Wang et al. 2011; Sahana et al. 2008). Heat treatment (annealing) is one other form of surface treatment that has proven to increase the crystallinity of hematite as well as the photocurrent (Kim et al. 2013).

There are several methods that can be employed in the preparation of microscopic hematite films. Amongst these, studies of hematite prepared by spray pyrolysis are very limited. Spray pyrolysis is a versatile method that can be varied and improved compared to conventional spray pyrolysis (Seo et al. 2006). It has been shown that films prepared by ultrasonic spray pyrolysis allow for better light-harvesting than those prepared by the conventional spray pyrolysis (Duret and Grätzel 2005). Herein, we report on the use of femtosecond pump-probe spectroscopy to investigate the electron–hole recombination rates resulting from the use of a larger spray volume, tetraethoxysilicate (TEOS) as a precursor, and the annealing of hematite. Confocal Raman microscopy was used to confirm the conformal and uniform

deposition of the thin films on the fluorine-doped tin oxide (FTO)-coated glass substrates. To the best of our knowledge, this is the first study on the combined effect of TEOS treatment and post-annealing on the recombination dynamics of hematite thin films.

Experimental

Sample preparation

The transparent hematite thin films were prepared on the fluorine-doped tin oxide-coated glass substrates by spraying a metal salt solution of Fe_2O_3 onto a heated substrate (Fig. 1). The setup entails a substrate heater, spray gun, air compressor, solution reservoir, and a gas exhaust gas unit (Thiagarajan et al. 2009).

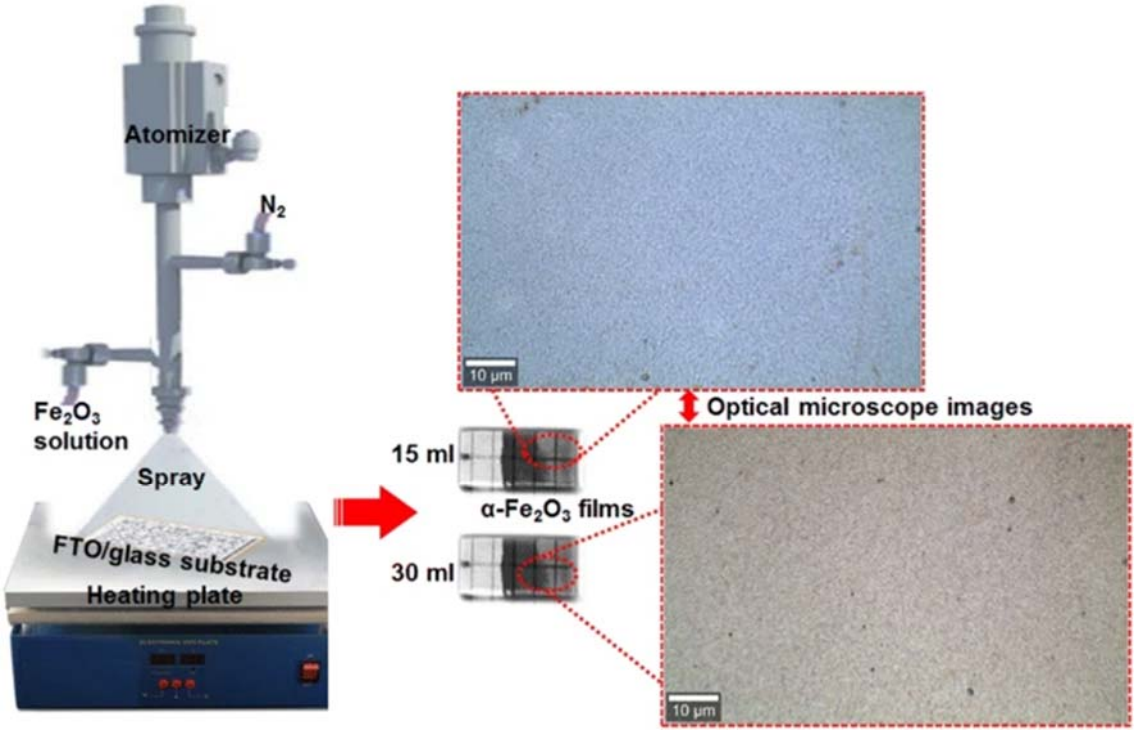

Fig. 1. Schematic diagram of the basic components of the spray pyrolysis setup with the optical microscope images of the 15 and 30 ml pristine α-Fe_2O_3 samples

In Fig. 1, the optical microscope images show the different hematite samples prepared by spray pyrolysis with Fe_2O_3 volumes of 15 ml and 30 ml. It is worth mentioning that the Fe_2O_3 spray volumes in the range ~ 10–30 ml exhibit continuous thin films with a negligible agglomeration of nanoparticles. From each spray volume of 15 ml and 30 ml, one sample was treated with tetraethoxysilicate (TEOS) without post-annealing (Sample 2) and another sample was post-annealed at 500 °C for 2 h with 10 °C/min ramping without TEOS treatment (Sample 3). The fourth sample from each volume set was both treated with TEOS and post-annealed to be compared to the untreated Sample 1 (see Table 1).

Table 1. Different hematite films prepared using 15 and 30 ml of the spray pyrolysis solution; and post-treated or untreated and annealed

15 ml				30 ml			
Sample 1	Sample 2	Sample 3	Sample 4	Sample 1	Sample 2	Sample 3	Sample 4
No	Yes	No	Yes	No	Yes	No	Yes
No	No	Yes	Yes	No	No	Yes	Yes

"Yes" means that the treatment has been applied

Characterization

Confocal Raman microscopy

A WITec alpha300 RAS + confocal Raman microscope [high-resolution confocal Raman imaging with integrated atomic force microscopy (AFM)] was used for analysis/imaging of the thin films. Acquisition of image scans and/or spectroscopy data was carried out using a 532 nm excitation laser (laser power of 5 mW) and × 100 Zeiss objective which gives a diffraction limited lateral and depth resolution of about 360 and 530 nm, respectively. The surface image scans were acquired over 40 × 40 μm^2 area and the depth profiles over a depth of 20 µm and a width of 30 µm with 100 points per line and 100 lines per image using an integration time of 3 s. For AFM imaging (AC mode), a × 20 Zeiss objective was used fitted with the cantilever with a spring constant of 2.8 N/m and a nominal resonance frequency of 75 kHz.

Transient absorption spectroscopy

Transient absorption (TA) spectroscopy measurements were performed using a Clark-MXR, Ti: Sapphire femtosecond laser source, which operates at a 1 kHz repetition rate with a pulse duration of 150 fs centered at 775 nm. The fundamental laser beam was split in two, referred to as the pump and probe beams. The pump beam was sent through a beta barium borate (BBO) crystal for frequency doubling, producing a beam centered at 387.5 nm. Using the spot size and pulse energy of the pump beam, the pump fluency at the sample was 1.02 mJ cm^{-2} $pulse^{-1}$. A chopper was placed in the path of the pump beam to block every second pulse, thus generating sequential pump-on and pump-off measurements. The probe beam was passed through a delay line with a total delay of up to 2 ns before being focused into a 4 mm sapphire crystal to produce a broad white light continuum in the visible wavelength range. The pump and probe beams were directed into the sample where they overlapped temporally, at time zero, and spatially. After the sample, the pump beam was blocked and the probe pulses were carefully aligned into a fiber cable connected to a spectrograph which dispersed the probe onto a CMOS sensor (Glaz LineScan-I, Synertronic Designs), so that the transmitted spectrum could be recorded. Measurements were performed using a custom-written MATLAB interface. Pump-probe measurements give difference absorption ($\Delta A = A_{pumped} - A_{unpumped}$) spectra. Glotaran software (Joly et al. 2006) was used to analyze the obtained data to find the evolution-associated difference spectra and associated decay lifetimes.

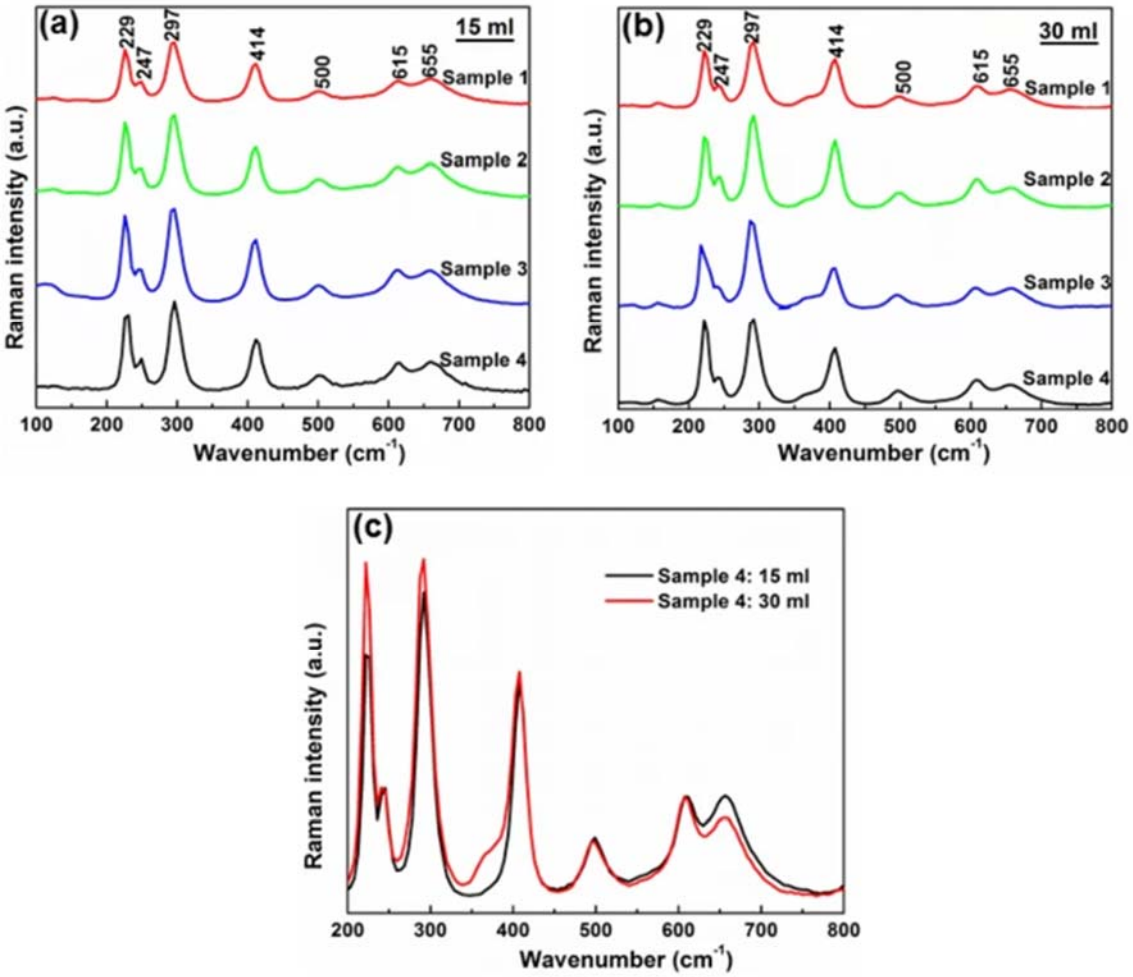

Fig. 2. Raman spectra of different hematite samples prepared by spray pyrolysis with a volume of **a** 15 ml and **b** 30 ml, for each spray volume, Sample 2 was post-treated, Sample 3 annealed, and Sample 4 was the combination of TEOS treatment and annealing. **c** Raman spectra of sample 4 for both 15 and 30 ml

Results and discussion

Confocal Raman microscopy

Amongst other characterization techniques, Raman spectroscopy is a preferred method for hematite analysis, since it is non-destructive and provides information on crystallinity, composition, and phase identification of different structures and the effect of disorder in films. Hematite has a corundum structure (Kang and Kang 2015), and for this structure, the group theory proposes seven first-order Raman-active vibrational modes, i.e., two A_{1g} and five E_g symmetries at the center of the Brillouin zone. Briefly, hematite has seven characteristic spectral features which are vibrational modes at 229, 247, 297, 302, 414, 500, and 615 cm^{-1} (see Fig. 2a, b). The vibrational modes at 229 and 500 are assigned to A_{1g} symmetry, while the other five modes (247, 297, 302, 414, and 615 cm^{-1}) are assigned to E_g symmetry. It can be seen from Fig. 2a, b that the as-prepared thin films exhibit the Raman characteristic spectral features of hematite material, as expected. In Fig. 2c, it can be seen that the Raman spectra of the films prepared using both 15 and 30 ml of the spray pyrolysis solution do not show peak-shifting, suggesting that the films have similar average particles

size (Bersani et al. 1998; Demopoulos et al. 2009; Gupta et al. 2009; Balaji et al. 2006; Jubb and Allen 2010). The films prepared using 30 ml of the spray pyrolysis solution display higher intensity peaks at 229 and 297 cm^{-1} compared to 15 ml samples (Fig. 2), suggesting that the 30 ml samples are slightly thicker than the 15 ml samples. Certainly, the intensity of the Raman scattering is proportional to the density of the interacting media.

To investigate the uniformity of the film on the FTO substrate, a Raman intensity map of the 297 cm^{-1} peak was obtained for each sample. Figure 3 shows the optical microscope images with an overlain Raman mapping for all the as-prepared samples. The uniform intensity of the mapping suggests a uniform composition (phase) of hematite across the analyzed areas of the samples. This suggests that a uniform coating of the hematite film was achieved on the substrates. In addition, the reduced surface roughness of the films seen from the optical microscope images confirms the uniform and conformal coverage across the FTO substrates.

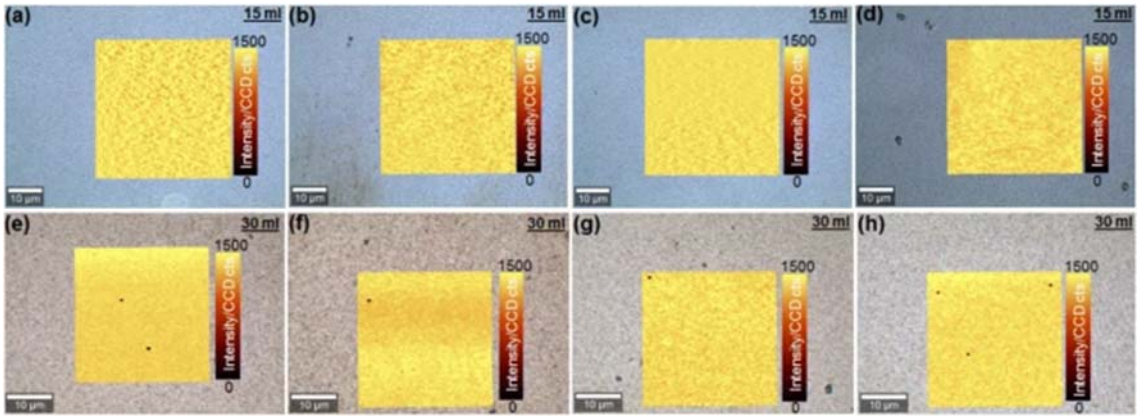

Fig. 3. Optical microscope images with an overlay Raman intensity mapping of the 297 cm^{-1} peak of different hematite samples prepared by spray pyrolysis with a volume of **a**–**d** 15 ml and **e**–**h** 30 ml, and post-treated or untreated and annealed

Moreover, the confocal Raman microscopy depth profiles were used to obtain the thickness of the prepared films by mapping the intensity of the 297 cm^{-1} peak of as-prepared hematite samples (see Fig. 4a–h). From the depth profiles, it can be seen that air and FTO/glass exhibit no signal with a phonon band at 297 cm^{-1}. Average depth line profiles were obtained (see Fig. 4I, j) and fitted with a Lorentzian function. The FWHM of the fitted curves represented the thickness of each as-prepared hematite film, as shown in Fig. 4k. The FWHM method (or 50% maximum intensity method) is used with the assumption that the actual interface appears at 50% of the maximum Raman intensity and the diffraction limited depth resolution at each interface is at best about 530 nm. From the thicknesses of the as-prepared hematite films for both 15 and 30 ml of the spray pyrolysis solution, it can be seen that the unannealed films (TEOS treated and untreated) display comparable thicknesses in the order of 800 nm. On the other hand, annealed films display thicknesses in the order of 600 nm. However, the films prepared using 30 ml of the spray pyrolysis solution show slightly thicker layers compared to the 15 ml solution.

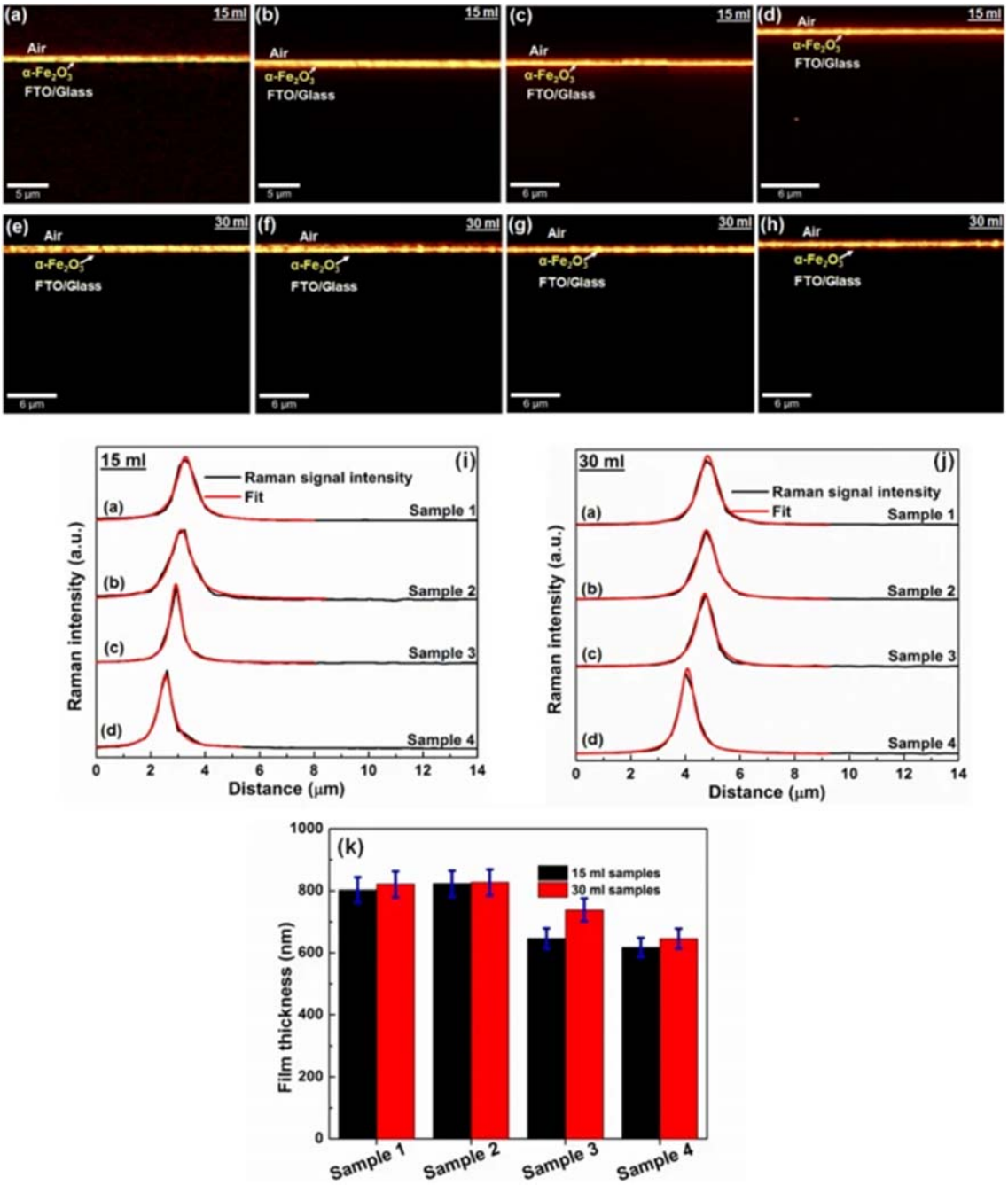

Fig. 4. Raman depth profiles (cross-section image) obtained by mapping the intensity of the 297 cm^{-1} peak of different hematite samples prepared by spray pyrolysis with a volume of **a**–**d** 15 ml and **e**–**h** 30 ml, where for each spray volume, Sample 2 was post-treated, Sample 3 annealed and Sample 4 was the combination of these two. **i**, **j** Average depth line profiles (black) corresponding with **a**–**h** and fitted with a Lorentzian function (red). **k** Thickness of the as-prepared hematite films for each of the samples for 15 ml (black) and 30 ml (red) of the spray pyrolysis solution

The surface roughness of the films was investigated using atomic force microscopy (AFM) and the results are presented in Fig. 5a–h. The average surface roughness values obtained from the AFM images of the films are plotted in Fig. 5i. The hematite films prepared using 15 ml of the spray pyrolysis solution display average surface roughness values (~ 6 nm) smaller than those prepared using 30 ml (~ 9 to 10 nm). Nonetheless, the reduced surface

roughness (< 10 nm) of the films further confirms the observed reduced roughness of the films from the optical microscope images which, in turn, confirms the uniform and conformal films coverage across the substrates. Moreover, the average particle size of the films was estimated from the AFM images (Fig. 5a–h) using brighter or higher intensity regions (color thresholding) with more particles (> 50) for better statistics, as shown in Fig. 5j. The unannealed and annealed films (TEOS untreated) for both 15 and 30 ml of the spray pyrolysis solution display a larger average particle size compared to the TEOS treated films (see Table 2). Also, the as-prepared films for 30 ml of the spray pyrolysis solution display a larger average particle size compared to the 15 ml samples as expected that the particle size would increase with the increase of the amount of Fe_2O_3 precursor, because the reactant with the higher amount enhances the merging of crystal nuclei and agglomeration of particles.

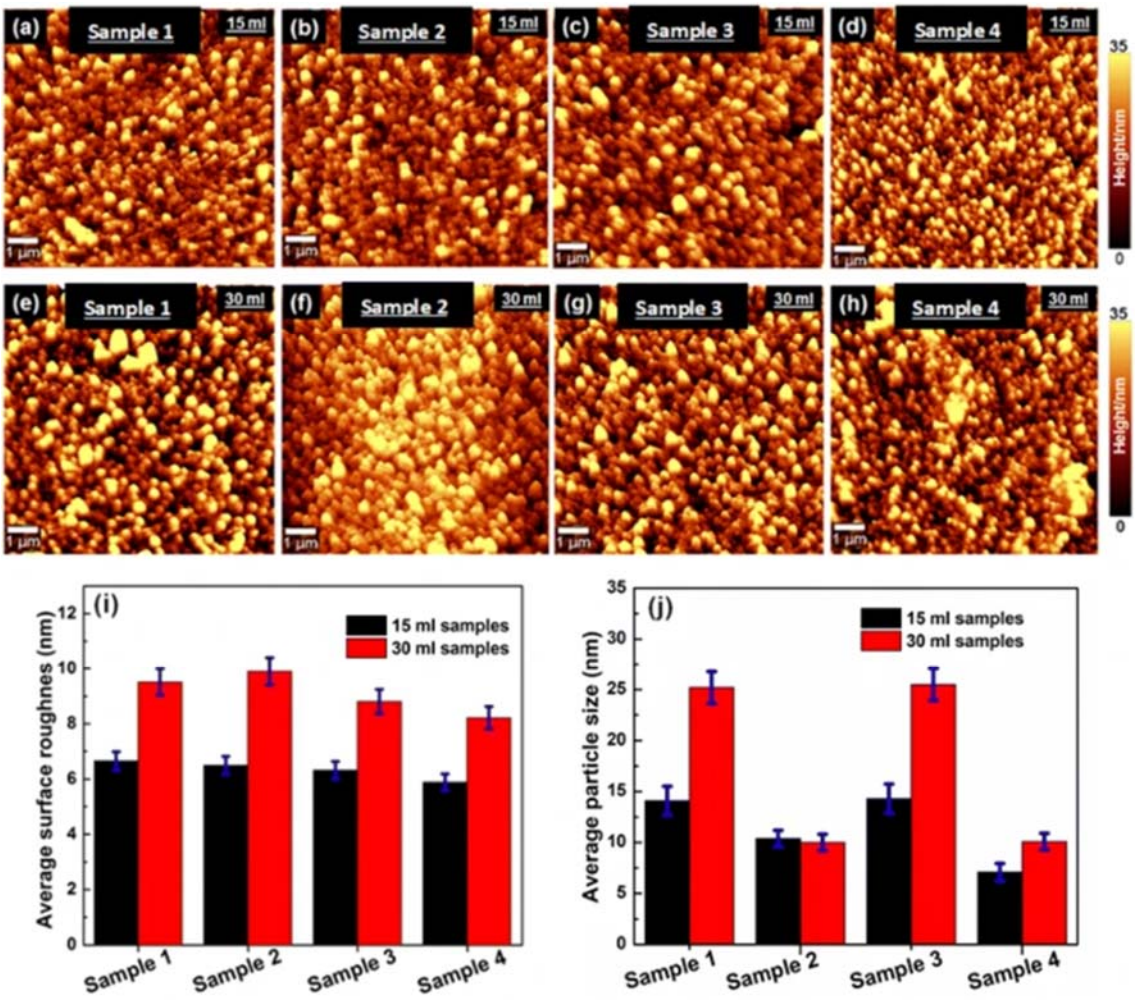

Fig. 5. a–**d** AFM surface images of different hematite samples prepared by spray pyrolysis with a volume of **a**–**d** 15 ml and **e**–**h** 30 ml, and post-treated or untreated and annealed. **i** Average surface roughness, corresponding to **a**–**h**. **j** Average particle size, corresponding to **a**–**h**

Table 2. Thicknesses, average surface roughness, and particles size of different hematite films prepared using 15 and 30 ml of the spray pyrolysis solution; and post-treated, annealed, and a combination of these two

Treatment	15 ml				30 ml			
	Sample 1	Sample 2	Sample 3	Sample 4	Sample 1	Sample 2	Sample 3	Sample 4
TEOS	No	Yes	No	Yes	No	Yes	No	Yes
Post-annealing @ 500 °C	No	No	Yes	Yes	No	No	Yes	Yes
Film thickness (nm)	802	822	646	617	820	826	738	645
Film roughness (nm)	6.7	6.5	6.3	5.9	9.5	9.9	8.8	8.2
Film particle size (nm)	14.1	10.4	14.3	7.1	25.2	10.0	25.5	10.1

Briefly, the thickness, surface roughness, and the particle size of the thin films changed significantly under treatment of TEOS and annealing. Treatment of both annealing and TEOS ultimately resulted in thinner and much smoother films (see Table 2).

Transient absorption spectroscopy

A two-dimensional transient absorption (TA) intensity map of pristine hematite films (i.e., sample 1 in Table 2 for 15 ml spray volume) is shown in Fig. 6. The measured TA signal is a sum of at least three contributions, namely, excited state absorption (ESA) of electrons and holes, ground-state bleach (GSB), and stimulated emission (SE). On the map, two time scales can be distinguished: fast decay of the broadband ESA signal within the first few ps, followed by a much slower decay of this signal within several tens of ps (Table 3). The main spectroscopic feature of this map is the ESA signal that peaks around 570 nm which is ascribed to absorption of mainly photo-generated holes (Pendlebury et al. 2011). All 8 samples have similar spectroscopic features which agree with earlier studies on hematite thin films (Huang et al. 2012; Paradzah et al. 2017).

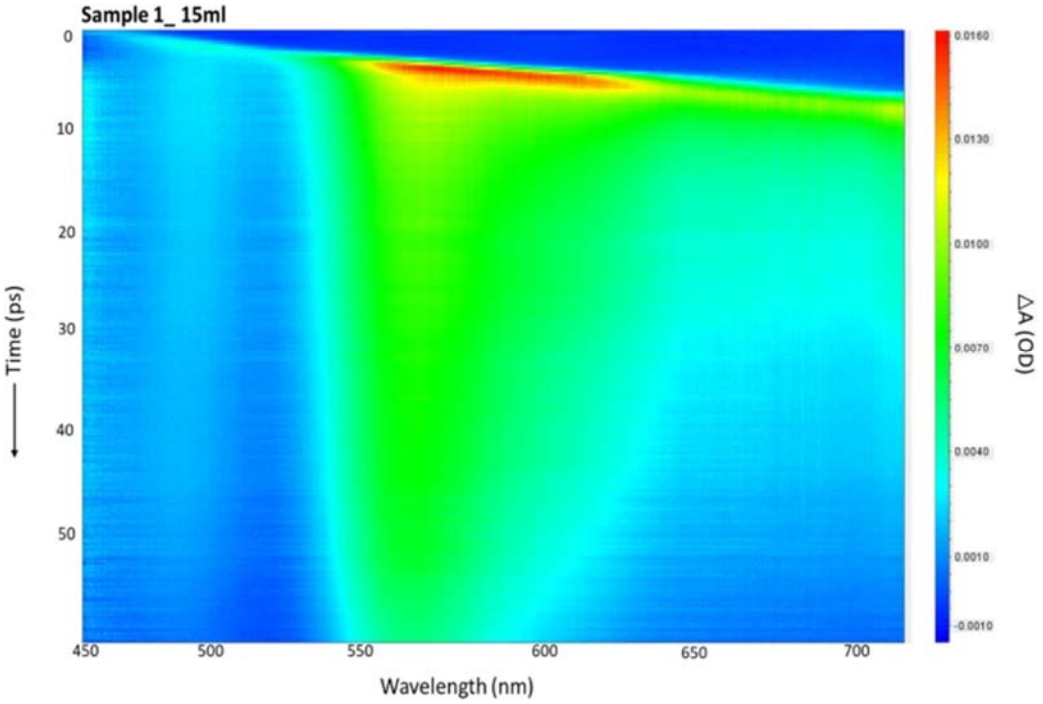

Fig. 6. Two-dimensional transient absorption intensity map of hematite sample 1 prepared by spray pyrolysis with a volume of 15 ml

Table 3 Decay lifetimes of the respective samples obtained from global analysis

Lifetimes	τ_1 (fs)	τ_2 (ps)	τ_3 (ps)
Spray pyrolysis volume 15 ml			
Sample 1	506	10.6	320
Sample 2	650	11.6	342
Sample 3	677	12.6	357
Sample 4	901	14.4	478
Spray pyrolysis volume 30 ml			
Sample 1	684	11.2	560
Sample 2	760	11.9	622
Sample 3	1332	19.7	703
Sample 4	1192	19.9	854

Global analysis

To study the ultrafast carrier dynamics of hematite, we used a three-component sequential kinetic scheme by analyzing the singular-value decomposition (SVD) parameters of the TA data. Each model component is characterized by an evolution-associated spectrum (EAS) and associated decay lifetime (Fig. 7a–h and Table 3). In all eight of the samples, an ultrafast initial component was resolved, which is attributed to the cooling of holes to the valence band maximum and electron cooling to the conduction band minimum (Joly et al. 2006). The second decay lifetimes range between ~ 10 and ~ 20 ps, and are attributed to recombination of electrons and holes as well as electron trapping by defect states and/or electronic levels (Cherepy et al. 1998). The third decay lifetimes range between 320 and 854 ps, and are attributed to recombination of conduction band electrons and valence band holes (Joly et al. 2006).

Considering only the samples prepared with 15 ml of hematite, the effect on the three decay lifetimes of three distinct experimental parameters was investigated. In every instant, each of the individual parameters prolonged each of the lifetimes and all combinations of the three parameters enhanced this effect. Hence, there is a clear individual and cumulative effect of all three experimental parameters. The first experimental parameter was treating pristine α-Fe_2O_3 with TEOS (sample 2), which led to a 1.2, 1.1, and 1.2 times decrease in the three decay rates (i.e., prolongment of the lifetimes) as compared to pristine α-Fe_2O_3 (sample 1). The TEOS chemical dopes hematite with silicon through the substitution of Fe^{3+} by Si^{4+} ions in the hematite lattice, which also results in a higher charge carrier concentration (Cesar et al. 2006). The doping of pristine hematite with Si as n-type dopant improves the photocurrent of porous films by improving charge transfer and also increases the hole diffusion length, thus prolonging the cooling of holes and electrons to the valence band maximum and conduction band minimum, respectively (Cesar et al. 2009; Chemelewski et al. 2012). Subsequently, this prolongs the recombination time of electrons and holes.

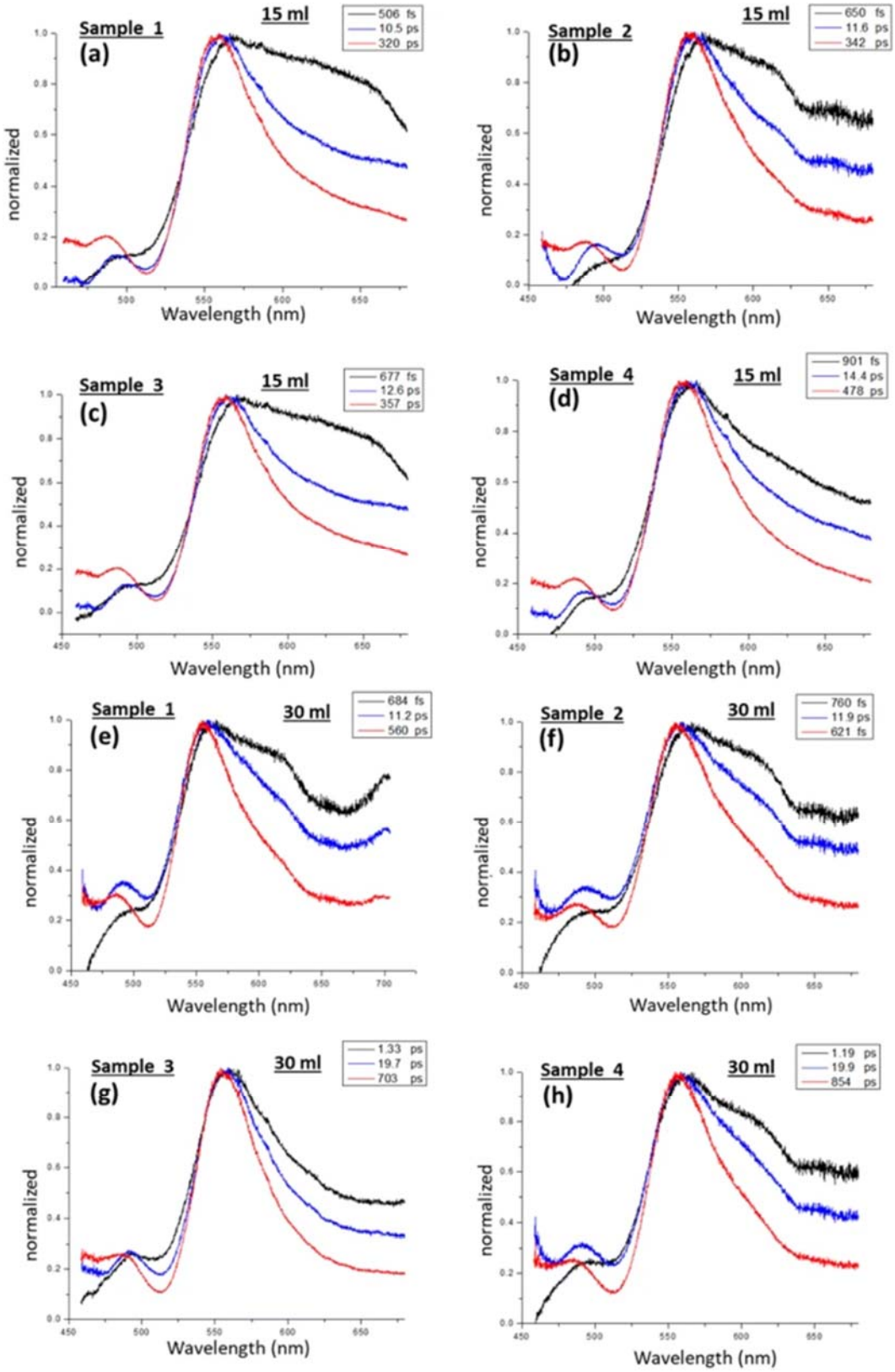

Fig. 7. Evolution-associated spectra of the eight thin-film hematite samples **a**–**d** 15 ml and **e**–**h** 30 ml obtained after SVD analysis of the TA raw data; where the black is the initial component, the blue line is the second component evolving from the first component, and the red line is the third component evolving from the second

The second experimental parameter was post-annealing of pristine α-Fe_2O_3 at 500 °C for 2 h with 10 °C/min ramping without TEOS treatment (Sample 3). We again observed a positive outcome with respect to the lifetimes. The three resolved decay rates of pristine α-Fe_2O_3 are, on average, a factor of 1.6, 1.5, and 1.3 times faster compared to those of the annealed hematite (sample 3). The prolonged lifetime of the charge carriers suggests reduced scattering of charge carriers due to the more spherical shape with well-defined borders formed by the nanostructures (Kim et al. 2013; Vasquez-Mansilla et al. 2001). The AFM images (Fig. 5a–d) confirm this, showing a reduction in the average particle size and surface roughness of sample 3 compared to sample 1. Since both TEOS treatment and annealing induced slower recombination rates independently, intuitively, one would expect the combination of the two treatments to reduce the recombination rates even further. This is confirmed by the results of Sample 4, showing that the three excitation decay rates are slowed down with a factor of ~ 1.8, 1.6, and 1.5, respectively, compared to those of sample 1.

The effect of doubling the volume of hematite used in the spray pyrolysis from 15 to 30 ml was also investigated. This effect caused a significant reduction in the recombination and other decay rates. Specifically, the three decay rates in pristine α-Fe_2O_3 prepared by spray pyrolysis with a volume of 15 ml are, on average, faster by ~ 1.5, 1.3, and 1.8, respectively, compared to those prepared with 30 ml. This can be attributed, but is not limited to the reduction in particle size with a better grain structure, as evidenced from Fig. 5a–h.

These results confirm that silicon-doped hematite has an improved photocurrent due to the slowing down of recombination. This suggests that elemental doping in some manner prolongs the decay lifetime of photoexcited charge carriers and, therefore, increases the solar-to-hydrogen conversion efficiency. Furthermore, the results also confirm that the annealing of hematite at certain temperatures improves the structure of the material and, as a result, reduces recombination. We also show that the use of a larger volume in spray pyrolysis can improve the crystallinity of the nanostructure and subsequently aid in slowing down recombination.

Conclusion

In this study, eight different hematite samples were prepared by spray pyrolysis on fluorine-doped tin oxide-coated glass substrates, of which four were treated with TEOS and the other four were left untreated. Of these samples, four were post-annealed (two that were TEOS treated and two that were untreated) at 500 °C for 2 h with 10 °C/min ramping. High-resolution confocal Raman microscopy with an integrated atomic force microscopy unit was used for analysis of the hematite thin films. For all the films, Raman spectroscopy confirmed the characteristic Raman spectrum of the hematite. The high-resolution Raman mapping confirmed a uniform coating of the hematite films on the FTO substrates. In addition, the reduced surface roughness of the films seen from the Raman optical microscope images as well as atomic force microscopy surface images confirmed the uniform and conformal coverage across the FTO substrates with the average surface roughness values in the order of < 10 nm. Moreover, from Raman depth profiles, the thicknesses of the films were obtained and ranged between 570 and 840 nm. Ultrafast transient absorption spectroscopy was used to resolve the carrier dynamics of the thin films. Upon global analysis of the raw TA data, EAS were obtained which gave the recombination rates of the different samples. Chemical treatment of TEOS, post-annealing, and increasing the spray volume led to a reduction in the recombination rates of photoexcited charge carriers on all resolved time scales, viz., 0.5–1.2 ps, 10.6–19.9 ps, and 320–854 ps.

Acknowledgements

Sipho Congolo acknowledges the financial support from University of Pretoria and National Research Foundation (NRF).

References

Seger B (2016) Global energy consumption: the numbers for now and in the future

Cho A (2010) Energy's tricky tradeoffs. Science 329:786–787. https://doi.org/10.1126/science.329.5993.786

Tadic M, Trpkov D, Kopanja L, Vojnovic S, Panjan M (2019) Hydrothermal synthesis of hematite (α-Fe2O3) nanoparticle forms: synthesis conditions, structure, particle shape analysis, cytotoxicity and magnetic properties. J Alloys Compd 792:599–609. https://doi.org/10.1016/j.jallcom.2019.03.414

Zhang Z, Huang S, Chen L, Wang B, Wen B, Zhang B, Guo D (2017a) Ultrahigh hardness on a face-centered cubic metal. Appl Surf Sci 416:891–900. https://doi.org/10.1016/j.apsusc.2017.04.223

Zhang Z, Cui J, Zhang J, Liu D, Yu Z, Guo D (2019) Environment friendly chemical mechanical polishing of copper. Appl Surf Sci 467–468:5–11. https://doi.org/10.1016/j.apsusc.2018.10.133

Zhang Z, Shi Z, Du Y, Yu Z, Guo L, Guo D (2018) A novel approach of chemical mechanical polishing for a titanium alloy using an environment-friendly slurry. Appl Surf Sci 427:409–415. https://doi.org/10.1016/j.apsusc.2017.08.064

Zhang Z, Cui J, Wang B, Wang Z, Kang R, Guo D (2017b) A novel approach of mechanical chemical grinding. J Alloys Compd 726:514–524. https://doi.org/10.1016/j.jallcom.2017.08.024

Zhang Z, Song Y, Xu C, Guo D (2012) A novel model for undeformed nanometer chips of soft-brittle HgCdTe films induced by ultrafine diamond grits. Scr Mater 67:197–200. https://doi.org/10.1016/j.scriptamat.2012.04.017

Wang B, Zhang Z, Chang K, Cui J, Rosenkranz A, Yu J, Lin C-T, Chen G, Zang K, Luo J, Jiang N, Guo D (2018) New deformation-induced nanostructure in silicon. Nano Lett 18:4611–4617. https://doi.org/10.1021/acs.nanolett.8b01910

S. Kumari, A.P. Singh, Sonal, D. Deva, R. Shrivastav, S. Dass, V.R. Satsangi, Spray pyrolytically deposited nanoporous Ti4+ doped hematite thin films for efficient photoelectrochemical splitting of water. Int. J. Hydrogen Energy. 35 (2010) 3985–3990. DOI: 10.1016/j.ijhydene.2010.01.101.

Huang Z, Lin Y, Xiang X, Rodríguez-Córdoba W, McDonald KJ, Hagen KS, Choi K-S, Brunschwig BS, Musaev DG, Hill CL, Wang D, Lian T (2012) In situ probe of photocarrier dynamics in water-splitting hematite (α-Fe_2O_3) electrodes. Energy Environ Sci 5:8923. https://doi.org/10.1039/c2ee22681b

Iandolo B, Wickman B, Zorić I, Hellman A (2015) The rise of hematite: origin and strategies to reduce the high onset potential for the oxygen evolution reaction. J Mater Chem A 3:16896–16912. https://doi.org/10.1039/C5TA03362D

Cho ES, Kang MJ, Kang YS (2015) Enhanced photocurrent density of hematite thin films on FTO substrates: effect of post-annealing temperature. Phys Chem Chem Phys 17:16145–16150. https://doi.org/10.1039/C5CP01823D

Dare-Edwards MP, Goodenough JB, Hamnett A, Trevellick PR (1983) Electrochemistry and photoelectrochemistry of Iron(II1) Oxide. J Chem Soc Faraday Trans I(79):2027–2041

Wang L, Palacios-Padrós A, Kirchgeorg R, Tighineanu A, Schmuki P (2014) Enhanced photoelectrochemical water splitting efficiency of a hematite-ordered Sb:SnO2 host-guest system. Chemsuschem 7:421–424. https://doi.org/10.1002/cssc.201301120

Satsangi VR, Kumari S, Singh AP, Shrivastav R, Dass S (2008) Nanostructured hematite for photoelectrochemical generation of hydrogen. Int J Hydrog Energy 33:312–318. https://doi.org/10.1016/j.ijhydene.2007.07.034

Beermann N, Vayssieres L, Lindquist S, Hagfeldt A (2000) Photoelectrochemical studies of oriented nanorod thin films of hematite. J Electrochem Soc 147:2456–2461

Shinde PS, Lee SY, Choi SH, Lee HH, Ryu J, Jang JS (2016) A synergistic effect of surfactant and ZrO2 underlayer on photocurrent enhancement and cathodic shift of nanoporous Fe_2O_3 photoanode. Sci Rep 6:32436. https://doi.org/10.1038/srep32436

Kim JY, Magesh G, Youn DH, Jang J-W, Kubota J, Domen K, Lee JS (2013) Single-crystalline, wormlike hematite photoanodes for efficient solar water splitting. Sci Rep 3:2681. https://doi.org/10.1038/srep02681

Shen S, Guo P, Wheeler DA, Jiang J, Lindley SA, Kronawitter CX, Zhang JZ, Guo L, Mao SS (2013) Physical and photoelectrochemical properties of Zr-doped hematite nanorod arrays. Nanoscale 5:9867. https://doi.org/10.1039/c3nr03245k

Wang D, Chen H, Chang G, Lin X, Zhang Y, Aldalbahi A, Peng C, Wang J, Fan C (2015) Uniform doping of titanium in hematite nanorods for efficient photoelectrochemical water splitting. ACS Appl Mater Interfaces 7:14072–14078. https://doi.org/10.1021/acsami.5b03298

Hahn NT, Mullins CB (2010) Photoelectrochemical performance of nanostructured Ti- and Sn-doped α-Fe_2O_3 photoanodes. Chem Mater 22:6474–6482. https://doi.org/10.1021/cm1026078

Paradzah AT, Diale M, Maabong K, Krüger TPJ (2017) Use of interfacial layers to prolong hole lifetimes in hematite probed by ultrafast transient absorption spectroscopy. Phys B Condens Matter. https://doi.org/10.1016/j.physb.2017.06.088

Miyake H, Kozuka H (2005) Photoelectrochemical properties of Fe_2O_3 −Nb_2O_5 films prepared by sol−gel method. J Phys Chem B 109:17951–17956. https://doi.org/10.1021/jp058051b

Hisatomi T, Dotan H, Stefik M, Sivula K, Rothschild A, Grätzel M, Mathews N (2012) Enhancement in the performance of ultrathin hematite photoanode for water splitting by an oxide underlayer. Adv Mater 24:2699–2702. https://doi.org/10.1002/adma.201104868

Kang MJ, Kang YS (2015) Ultrathin insulating under-layer with a hematite thin film for enhanced photoelectrochemical (PEC) water splitting activity. J Mater Chem A 3:15723–15728. https://doi.org/10.1039/C5TA03468J

Wang G, Ling Y, Wheeler DA, George KEN, Horsley K, Heske C, Zhang JZ, Li Y (2011) Facile synthesis of highly photoactive α-Fe_2 O_3 -based films for water oxidation. Nano Lett 11:3503–3509. https://doi.org/10.1021/nl202316j

Sahana MB, Sudakar C, Setzler G, Dixit A, Thakur JS, Lawes G, Naik R, Naik VM, Vaishnava PP (2008) Bandgap engineering by tuning particle size and crystallinity of SnO_2–Fe_2O_3 nanocrystalline composite thin films. Appl Phys Lett 93:231909. https://doi.org/10.1063/1.3042163

Seo DJ, Cho MY, Park SB (2006) Preparation of titania nanoparticles of anatase phase by using flame spray pyrolysis. Stud Surf Sci Catal 159:761–764. https://doi.org/10.1016/S0167-2991(06)81708-8

Duret A, Grätzel M (2005) Visible light-induced water oxidation on mesoscopic α-Fe_2O_3 films made by ultrasonic spray pyrolysis. J Phys Chem B 109:17184–17191. https://doi.org/10.1021/jp044127c

Thiagarajan R, Anusuya M, Beevi MM (2009) Mechanical characterization of spray pyrolytic cadmium sulphide thin films by indentation technique. J Am Sci 5:51–56

Joly AG, Williams JR, Chambers SA, Xiong G, Hess WP, Laman DM (2006) Carrier dynamics in (0001) thin films and single crystals probed by femtosecond transient absorption and reflectivity. Cit J Appl Phys 99:144305. https://doi.org/10.1063/1.1869492

Bersani D, Lottici PP, Ding X-Z (1998) Phonon confinement effects in the Raman scattering by TiO_2 nanocrystals. Appl Phys Lett 72:73. https://doi.org/10.1063/1.120648

Demopoulos GP, Charbonneau C, Lee K, Shan G, Gomez MA, Gauvin R (2009) Synthesis of hydroxyl-rich anatase nanocrystallites, their characterization and performance as photoanode in dye-sensitized solar cells. ECS Trans. **(**The Electrochemical Society**)**. https://doi.org/10.1149/1.3271672

Gupta SK, Desai R, Jha PK, Sahoo S, Kirin D (2009) Titanium dioxide synthesized using titanium chloride: size effect study using Raman spectroscopy and photoluminescence. J. Raman Spectrosc. https://doi.org/10.1002/jrs.2427

Balaji S, Djaoued Y, Robichaud J (2006) Phonon confinement studies in nanocrystalline anatase-TiO_2 thin films by micro Raman spectroscopy. J Raman Spectrosc 37:1416–1422. https://doi.org/10.1002/jrs.1566

Jubb AM, Allen HC (2010) Vibrational spectroscopic characterization of hematite, maghemite, and magnetite thin films produced by vapor deposition. ACS Appl Mater Interfaces 2:2804–2812. https://doi.org/10.1021/am1004943

Pendlebury SR, Barroso M, Cowan AJ, Sivula K, Tang J, Grätzel M, Klug D, Durrant JR (2011) Dynamics of photogenerated holes in nanocrystalline α-Fe_2O_3 electrodes for water oxidation probed by transient absorption spectroscopy. Chem Commun. https://doi.org/10.1039/C0CC03627G

Cherepy NJ, Liston DB, Lovejoy JA, Deng H, Zhang JZ (1998) Ultrafast studies of photoexcited electron dynamics in γ-and r-Fe_2O_3 semiconductor nanoparticles

Cesar I, Kay A, Gonzalez Martinez JA, Grä M (2006) Translucent Thin Film Fe2O3 Photoanodes for efficient water splitting by sunlight: nanostructure-directing effect of Si-doping. J Am Chem Soc 128:4582–4583. https://doi.org/10.1021/ja060292p

Cesar I, Sivula K, Kay A, Zboril R, Grätzel M (2009) Influence of feature size, film thickness, and silicon doping on the performance of nanostructured hematite photoanodes for solar water splitting. J Phys Chem C 113:772–782. https://doi.org/10.1021/jp809060p

Chemelewski WD, Hahn NT, Mullins CB (2012) Effect of Si doping and porosity on hematite's (α-Fe_2O_3) photoelectrochemical water oxidation performance. J Phys Chem C 116:5255–5261. https://doi.org/10.1021/jp210877u

Vasquez-Mansilla M, Zysler RD, Arciprete C, Dimitrijewits M, Rodriguez-Sierra D, Saragovi C (2001) Annealing effects on structural and magnetic properties of α-Fe2O3 nanoparticles. J Magn Magn Mater 226–230:1907–1909. https://doi.org/10.1016/S0304-8853(00)00858-1